Chiral anomaly in type-I Weyl semimetals: Comprehensive analysis within a semiclassical Fermi surface harmonics approach

Annika Johansson,[1,2,*] Jürgen Henk,[2] and Ingrid Mertig[2,1]

[1]*Max Planck Institute of Microstructure Physics, Weinberg 2, 06120 Halle, Germany*
[2]*Institute of Physics, Martin Luther University Halle-Wittenberg, 06099 Halle, Germany*

In Weyl semimetals, the chiral charge is not conserved in the presence of external nonorthogonal magnetic and electric fields; this chiral anomaly manifests itself in a negative longitudinal magnetoresistance. In this paper, we report on detailed calculations of transport properties of type-I Weyl semimetals with broken time-reversal and broken inversion symmetries, respectively, within a semiclassical Boltzmann approach. The use of Fermi surface harmonics provides a comprehensive and closed solution of the Boltzmann equation including the influence of the Lorentz force as well as **k**-dependent scattering-out and scattering-in terms. Respecting a modified phase space volume, we identify additional contributions to the charge conductivity, which scale linearly with the magnetic field and can change the sign of the magnetoresistance in systems with broken inversion symmetry. Considering the scattering properties, the energy dependence of the chiral anomaly-related contribution to the charge conductivity is more pronounced than usually discussed. On top of this, we show for the Weyl semimetal TaAs that a misalignment of an applied magnetic field with the crystal axes can destroy the negative longitudinal magnetoresistance.

I. INTRODUCTION

Weyl semimetals (WSMs) [1–5] have attracted high attention in the last few years due to their unique physical properties related to the topological character of their bulk band structure. Kramers degeneracy is lifted because at least one of the two symmetries—time-reversal or inversion—is broken. The conduction and valence bands touch at special singular twofold degenerate points $\mathbf{k}_W$, called Weyl points, at which the bands disperse linearly in all three directions in reciprocal space. Hence, the bands close to the Weyl points can be described by the Weyl Hamiltonian

$$\hat{H}_\chi(\mathbf{k}) = \chi \hbar v_0 (\mathbf{k} - \mathbf{k}_W) \cdot \hat{\boldsymbol{\sigma}}. \qquad (1)$$

Here, $\chi = \pm 1$ is the chirality of the Weyl point, $\hat{\boldsymbol{\sigma}}$ is in general a pseudospin related to the conduction and valence bands, and v_0 characterizes the group velocity around the Weyl point.

WSMs are commonly interpreted as a solid-state realization of Weyl fermions [6]. In solids, Weyl points always occur in pairs, with partners of opposite chirality [7–9]. Corresponding to their chirality, they are either monopoles or antimonopoles of Berry curvature and carry a topological charge χ. This topological property gives rise to topological surface states that connect the projections of the Weyl points onto the surface Brillouin zone; their Fermi lines are called Fermi arcs [2].

Due to their topologically nontrivial character, WSMs provide promising transport properties, for example, a large anomalous Hall effect [2,10,11] and a recently predicted

large current-induced spin polarization originating from the surface states [12]. However, their characterizing effect is the Adler-Bell-Jackiw chiral anomaly [13–15], originally discussed in high-energy physics. In the presence of nonorthogonal magnetic (**B**) and electric (**E**) fields, the number of states with a distinct chirality (or chiral charge) is not conserved. For WSMs, the chiral anomaly is discussed either in the ultraquantum limit, in which Landau quantization leads to chiral linear modes [15], or in the semiclassical limit for small magnetic fields and nonzero Fermi energy [16,17]. The chiral anomaly causes an additional contribution to the longitudinal (parallel to **B**) charge conductivity, which scales with B in the ultraquantum limit and with B^2 in the semiclassical limit [15,16]. A detection of the resulting negative longitudinal magnetoresistance (NLMR) is therefore often considered a strong hint for the existence of Weyl points. However, since the chiral anomaly is not the only origin of a NLMR [18], other phenomena causing NLMR have to be excluded to identify clearly a Weyl semimetal. Considering the above, it is self-evident that the chiral anomaly in Weyl semimetals is subject of theoretical and experimental investigations [18–28].

The aim of this work is to provide a full semiclassical consideration of the transport properties in WSMs, which includes all charge conductivity tensor elements. For the discussion of the chiral anomaly within the semiclassical Boltzmann theory, usually the Lorentz force term as well as scattering-in terms are neglected in order to solve the Boltzmann equation analytically [16,17,24–26]. These approximations are sufficient as long as only the longitudinal charge conductivity is calculated. In our calculations, including the Lorentz force is crucial since it strongly influences the transversal as well as the diagonal tensor elements which are not aligned with **B**.

An efficient way of solving the linearized Boltzmann equation including the influence of the Lorentz force as well as energy- and **k**-dependent scattering-out and scattering-in terms is provided by the method of Fermi surface harmonics (FSHs) [29–31], which will be applied in this paper. To include Berry curvature effects and the nonconservation of phase space volume, which is due to the nontrivial topology and is important especially for energies close to the Weyl points [32], the established FSH formalism is extended.

In a seminal paper [16], Son and Spivak discussed the chiral anomaly in the semiclassical limit by modeling a pair of Weyl points by two copies of the Weyl Hamiltonian (1). Here, we describe Weyl pairs by an anisotropic Hamiltonian. This inherent anisotropy produces additional contributions to the charge conductivity, which can modify the LMR quantitatively as well as qualitatively; it even allows for a change of sign [24–26]. On top of this, the energy and **k** dependencies of the scattering term in the Boltzmann equation modify the energy dependence of the transport coefficients.

Whereas the chiral anomaly is often discussed for systems of two or four Weyl points [16,17,24–26], we systematically increase the number of Weyl points considering system of two, four and 24 Weyl points. We elaborate on the influence of inversion and time-reversal symmetry on the transport properties, respectively, and demonstrate that an increased number of Weyl points reduces anisotropy effects.

Experimental data [18–22] often show a positive longitudinal magnetoresistance (PLMR) for small magnetic fields, which is usually attributed to weak antilocalization effects [33]. At medium scale magnetic fields, the LMR signal is negative and in good agreement with the semiclassical theory. These findings call to recognize other reasons leading to a PLMR in the semiclassical limit. In this work, we identify such mechanisms. More precisely, in anisotropic systems with broken time-reversal symmetry additional contributions $\propto B$ to the charge conductivity (Refs. [24–26]) can change the sign of the LMR; these appear in addition to the conventional terms $\propto B^2$ (Ref. [16]). Further, transport transversal to the magnetic field can also modify the LMR due to the Lorentz force. In particular, slightly misaligned external electric and magnetic fields give rise to qualitative deviations from the LMR that has been discussed in Ref. [16]; furthermore, such misalignment may result in a sign change.

The paper is organized as follows. In Sec. II, a two-band model Hamiltonian proposed by Okugawa and Murakami [34,35] is presented, which will be used throughout the paper to describe Weyl pairs. The method of Fermi surface harmonics for solving the semiclassical Boltzmann transport equation is introduced in Sec. III. Section IV gives an overview of the contributions to the charge current in systems with nonzero Berry curvature in the presence of external electric and magnetic fields. In Sec. V, the theory is applied to calculate the charge conductivity as well as the magnetoresistance in model systems of two (broken time-reversal symmetry) and four (broken inversion symmetry) Weyl points. Finally, the model Hamiltonian is extended to the realistic Weyl semimetal TaAs. The transport properties are calculated and related to the experimental results of Zhang *et al.* [18].

II. TWO-BAND MODEL FOR A PAIR OF WEYL POINTS

The Weyl Hamiltonian (1) approximates the band structure close to a single Weyl point. Modeling a Weyl pair by two copies of this Hamiltonian leaves these two isotropic band-structures unconnected. In real systems, however, the bands of a Weyl pair are connected at energies away from the Weyl point energy; therefore, anisotropies occur. To model the band structure more realistically, we use the two-band Hamiltonian proposed by Okugawa and Murakami [34,35] for a pair of Weyl points but in the slightly modified version [12]

$$\hat{H}_p(\mathbf{k}) = p\gamma\left(k_{p,x}^2 - m\right)\hat{\sigma}_y + \hbar(v_z k_{p,z}\hat{\sigma}_z - v_y k_{p,y}\hat{\sigma}_x). \quad (2)$$

$\hat{\boldsymbol{\sigma}}$ is the pseudospin of valence and conduction band, $p = \pm 1$ is the Weyl pair index and $\mathbf{k}_p = \mathbf{k} - p\mathbf{k}_0$. The parameters γ, m, v_y, and v_z model the material-specific properties of the band structure. In the following, $m > 0$.

The energy dispersion

$$\mathcal{E}_p^v(\mathbf{k}) = v\sqrt{\gamma^2\left(k_{p,x}^2 - m\right)^2 + \hbar^2\left(v_y^2 k_{p,y}^2 + v_z^2 k_{p,z}^2\right)} \quad (3)$$

($v = \pm 1$) and constant-energy surfaces are depicted in Fig. 1. The dispersion is almost linear around the Weyl points, which are located at $\mathbf{k}_W = p\mathbf{k}_0 \pm (\sqrt{m}, 0, 0)$. The two Weyl cones are connected at saddle points with energies $\pm\mathcal{E}_S = \pm\gamma m$. There, a Lifshitz transition from a double-sheet ($|\mathcal{E}| < |\mathcal{E}_S|$) to a single-sheet Fermi surface ($|\mathcal{E}| > |\mathcal{E}_S|$) occurs, which is accompanied by a change of the Fermi surface chirality from $\chi = \pm 1$ to $\chi = 0$.

A single Weyl pair can be realized in systems with inversion symmetry and broken time-reversal symmetry. There, the index p determines the orientation of the Weyl dipole moment [36], which is given by the distribution of the Weyl points' chiralities in reciprocal space. For a time-reversal invariant system with broken inversion symmetry, the minimum number of Weyl pairs is two, which requires one copy of the Hamiltonian (2) with $p = 1$ and another copy with $p = -1$; a detailed discussion is given in Ref. [12]. A higher number of Weyl pairs demands more Hamiltonian copies, which have to be positioned in reciprocal space in accordance with the system's spatial symmetries.

III. SEMICLASSICAL BOLTZMANN EQUATION AND FERMI SURFACE HARMONICS

A. Boltzmann equation

Within the semiclassical limit, the temporal evolution of the distribution function $f_{\mathbf{k}}(\mathbf{r}, t)$ of an electronic system under the influence of external fields as well as potential and temperature gradients is expressed by the Boltzmann transport equation

$$\frac{\partial f_{\mathbf{k}}(\mathbf{r}, t)}{\partial t} + \dot{\mathbf{k}}\nabla_{\mathbf{k}} f_{\mathbf{k}}(\mathbf{r}, t) + \dot{\mathbf{r}}\nabla_{\mathbf{r}} f_{\mathbf{k}}(\mathbf{r}, t) = \left(\frac{\partial f_{\mathbf{k}}(\mathbf{r}, t)}{\partial t}\right)_{\text{sc}}, \quad (4)$$

which comprises the field term $\dot{\mathbf{k}}\nabla_{\mathbf{k}} f_{\mathbf{k}}(\mathbf{r}, t)$, the diffusion term $\dot{\mathbf{r}}\nabla_{\mathbf{r}} f_{\mathbf{k}}(\mathbf{r}, t)$, and the scattering term

$$\left(\frac{\partial f_{\mathbf{k}}(\mathbf{r}, t)}{\partial t}\right)_{\text{sc}} = \sum_{\mathbf{k}'}\left(P_{\mathbf{k}\leftarrow\mathbf{k}'}g_{\mathbf{k}'} - P_{\mathbf{k}'\leftarrow\mathbf{k}}g_{\mathbf{k}}\right). \quad (5)$$
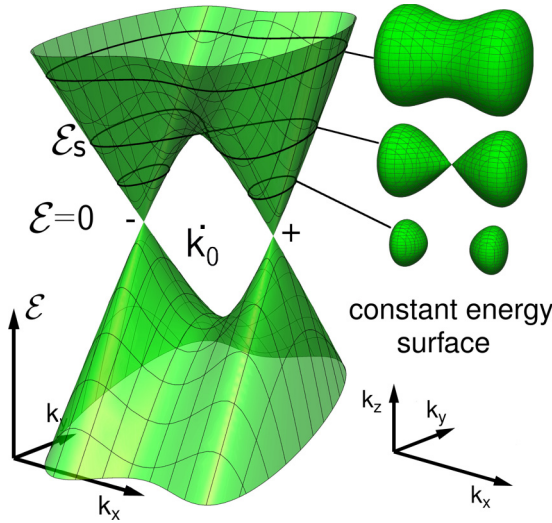
FIG. 1. Electronic structure of a Weyl pair modeled by the Hamiltonian Eq. (2) (schematic). (Left) Band structure as given by Eq. (3). At the saddle points with energies $\pm\mathcal{E}_S$, the Fermi surfaces undergo a Lifshitz transition from two sheets with $\chi = \pm 1$ to one sheet with $\chi = 0$. (Right) Surfaces of selected constant energies, as indicated.

Here, $P_{\mathbf{k}'\leftarrow\mathbf{k}}$ is the microscopic probability rate for transitions from state $|\mathbf{k}\rangle$ to state $|\mathbf{k}'\rangle$, $g_{\mathbf{k}}(\mathbf{r}, t) = f_{\mathbf{k}}(\mathbf{r}, t) - f_{\mathbf{k}}^0(\mathbf{r}, t)$ is the nonequilibrium deviation from the equilibrium distribution function $f_{\mathbf{k}}^0(\mathbf{r}, t)$ (Fermi-Dirac distribution). $P_{\mathbf{k}\leftarrow\mathbf{k}'}g_{\mathbf{k}'}$ and $P_{\mathbf{k}'\leftarrow\mathbf{k}}g_{\mathbf{k}}$ are called scattering-in and scattering-out terms, respectively.

The semiclassical equations of motion [37]

$$\dot{\mathbf{k}} = -\frac{e}{\hbar}\mathbf{E} - \frac{e}{\hbar}\dot{\mathbf{r}} \times \mathbf{B},$$

$$\dot{\mathbf{r}}_{\mathbf{k}} = \mathbf{v}_{\mathbf{k}} - \dot{\mathbf{k}} \times \mathbf{\Omega}_{\mathbf{k}}, \tag{6}$$

relate $\dot{\mathbf{k}}$ and $\dot{\mathbf{r}}_{\mathbf{k}}$ to the external fields and the electronic structure. The first equation is Newton's second axiom for the Lorentz force ($e > 0$ elementary charge), while the second equation contains the group velocity $\mathbf{v}_{\mathbf{k}} = \nabla_{\mathbf{k}}\mathcal{E}_{\mathbf{k}}/\hbar$ and the anomalous velocity originating from the Berry curvature $\mathbf{\Omega}_{\mathbf{k}}$.

In the following, we consider a stationary and spatially homogeneous system at zero temperature. By decoupling Eq. (6), we rewrite the Boltzmann equation as

$$-\frac{e}{\hbar}\eta_{\mathbf{k}}(\mathbf{B})^{-1}\left[\mathbf{E} + \mathbf{v}_{\mathbf{k}} \times \mathbf{B} + \frac{e}{\hbar}(\mathbf{E} \cdot \mathbf{B}) \cdot \mathbf{\Omega}_{\mathbf{k}}\right]\nabla_{\mathbf{k}}f_{\mathbf{k}}$$

$$= \left(\frac{\partial f_{\mathbf{k}}(\mathbf{r}, t)}{\partial t}\right)_{\text{sc}}, \tag{7}$$

with the definition

$$\eta_{\mathbf{k}}(\mathbf{B}) \equiv 1 + \frac{e}{\hbar}\mathbf{B} \cdot \mathbf{\Omega}_{\mathbf{k}}. \tag{8}$$

The nonequilibrium distribution function is written as

$$g_{\mathbf{k}} = \frac{\partial f_{\mathbf{k}}^0}{\partial \mathcal{E}_{\mathbf{k}}}e\mathbf{\Lambda}_{\mathbf{k}} \cdot \mathbf{E}, \tag{9}$$

considering only terms linear in $\mathbf{E}$ ($\mathbf{\Lambda}_{\mathbf{k}}$ mean free path). By assuming only elastic scattering Eq. (7) becomes linearized,

that is

$$\mathbf{\Lambda}_{\mathbf{k}} - \frac{e}{\hbar}\tau_{\mathbf{k}}\,\eta_{\mathbf{k}}^{-1}(\mathbf{B})[(\mathbf{v}_{\mathbf{k}} \times \mathbf{B}) \cdot \nabla_{\mathbf{k}}]\mathbf{\Lambda}_{\mathbf{k}}$$

$$= \tau_{\mathbf{k}}\left\{\eta_{\mathbf{k}}^{-1}(\mathbf{B})\left[\mathbf{v}_{\mathbf{k}} + \frac{e}{\hbar}(\mathbf{\Omega}_{\mathbf{k}} \cdot \mathbf{v}_{\mathbf{k}}) \cdot \mathbf{B}\right] + \sum_{\mathbf{k}'}P_{\mathbf{k}\leftarrow\mathbf{k}'}\mathbf{\Lambda}_{\mathbf{k}'}\right\}. \tag{10}$$

The inverse momentum relaxation time

$$\tau_{\mathbf{k}}^{-1} = \sum_{\mathbf{k}'}P_{\mathbf{k}'\leftarrow\mathbf{k}} \tag{11}$$

is calculated from the microscopic transition probability rates using Fermi's golden rule

$$P_{\mathbf{k}'\leftarrow\mathbf{k}} = \frac{2\pi}{\hbar}|T_{\mathbf{k}'\leftarrow\mathbf{k}}|^2\delta(\mathcal{E}_{\mathbf{k}} - \mathcal{E}_{\mathbf{k}'}) \tag{12}$$

for elastic scattering. The transition matrix elements

$$T_{\mathbf{k}'\leftarrow\mathbf{k}} = \langle\mathbf{k}'|\,\Delta V\,|\mathbf{k}\rangle \tag{13}$$

are calculated in Born approximation, in which the scattering potential

$$\Delta V(\mathbf{r}) = UV_0^{(d)}\sum_j \delta(\mathbf{r} - \mathbf{R}_j) \tag{14}$$

is a sum over δ-shaped impurity potentials at positions $\mathbf{R}_j$ and with scattering strength U. The latter is taken independent from $\mathbf{k}$ and identical for all impurities ($V_0^{(d)}$ volume of the unit cell in d dimensions; here, $d = 3$).

To account for inter- as well as intracone scattering processes, the Boltzmann equation is solved for each state $|\mathbf{k}\rangle$. As a consequence, the momentum relaxation time $\tau_{\mathbf{k}}$ depends on $\mathbf{k}$ and $\mathcal{E}$. These dependencies remarkably influence the energy dependence of the transport properties, in particular the chiral anomaly-related charge conductivity discussed below. Recall that in Ref. [16], the Boltzmann equation is transformed into a Weyl-cone-dependent form containing the intercone momentum relaxation time as a constant parameter.

Eventually, the charge current density

$$\mathbf{j}_{\text{c}} = -\frac{e}{V^{(d)}}\sum_{\mathbf{k}}\dot{\mathbf{r}}_{\mathbf{k}}f_{\mathbf{k}} \tag{15}$$

is a sum over all states that can be transformed into an integration in $\mathbf{k}$ space ($V^{(d)}$ volume of the system).

B. Phase space correction

In the presence of a nonzero Berry curvature and a magnetic field, the volume of an element in the $2d$-dimensional phase space that is spanned by $\mathbf{k}$ and $\mathbf{r}$ is not conserved during the temporal evolution [32]. The joint effect of Berry curvature and magnetic field can be interpreted as a deformation of the phase space, slightly changing the isoenergy surfaces in reciprocal space. In order to compensate for this deformation, the density of states has to be corrected [32]. For example, the $\mathbf{k}$ sum in Eq. (15) is replaced by a $\mathbf{k}$ integration,

$$\sum_{\mathbf{k}} \rightarrow \frac{V^{(d)}}{(2\pi)^d}\int d^3k\,\eta_{\mathbf{k}}(\mathbf{B}). \tag{16}$$

The correction factor $\eta_{\mathbf{k}}$, defined in Eq. (8), enters the Boltzmann equation (10); it cannot be safely neglected in phase space regions with large Berry curvature, that is close to the Weyl points.

C. Fermi surface harmonics

The method of Fermi surface harmonics (FSHs) [29–31] provides a closed solution of Eq. (10) in the presence of electric as well as magnetic fields. The FSHs are a set of functions that are orthonormal on the chosen isoenergy surface (here Fermi surface). They are constructed from the Cartesian components of the Fermi velocity,

$$\Psi_M(\mathbf{k}) = v_x^{n_x}(\mathbf{k}) \, v_y^{n_y}(\mathbf{k}) \, v_z^{n_z}(\mathbf{k}) \, \xi_{n_{\mathrm{FS}}}(\mathbf{k}). \qquad (17)$$

The multi-index $M = (n_x, n_y, n_z, n_{\mathrm{FS}})$ comprises the integers $n_x, n_y, n_z \geqslant 0$ and $n_{\mathrm{FS}} > 0$. $N_{\mathrm{FSH}} = n_x + n_y + n_z$ is the order of the FSH. For a multisheeted Fermi surface, the number of FSHs has to be increased correspondingly, which is provided by the Fermi surface sheet index n_{FS}.

The weights $\xi_{n_{\mathrm{FS}}}(\mathbf{k})$ ensure the orthogonality of FSHs that belong to different Fermi surface sheets. In this paper, we use the disjoint FSH representation: $\xi_{n_{\mathrm{FS}}}$ are chosen to guarantee that each FSH is nonzero only on one Fermi sheet; FSHs with different indices n_{FS} do not overlap [29]. In comparison to the symmetric representation, in which each FSH is defined on all Fermi sheets, this disjoint representation has the advantages that it is numerically efficient and intuitive.

For an isotropic system, the FSHs in the first Brillouin zone are identical to the spherical harmonics. The latter do not obey the periodicity of the reciprocal lattice and are not orthonormal for arbitrary Fermi surfaces.

In order to solve the linearized Boltzmann equation (10), the $\mathbf{k}$ and $\mathbf{B}$ dependencies of $\boldsymbol{\Lambda}_{\mathbf{k}}(\mathbf{B})$ have to be separated, which is accomplished by the ansatz

$$\boldsymbol{\Lambda}_{\mathbf{k}}(\mathbf{B}) = \sum_M \boldsymbol{\Lambda}_M(\mathbf{B}) \Psi_M(\mathbf{k}). \qquad (18)$$

The Boltzmann equation can then be written as a system of linear equations,

$$\sum_{M'} (\mathcal{B}_{MM'} + \mathcal{C}_{MM'}) \boldsymbol{\Lambda}_{M'}(\mathbf{B}) = \mathbf{D}_M. \qquad (19)$$

The field term matrix

$$\mathcal{B}_{MM'} = - N^{-1}(\mathcal{E}_{\mathrm{F}}) \sum_{\mathbf{k}} \delta(\mathcal{E}_{\mathbf{k}} - \mathcal{E}_{\mathrm{F}}) \Psi_M(\mathbf{k})$$

$$\times \tau_{\mathbf{k}} \, \eta_{\mathbf{k}}^{-1}(\mathbf{B}) \frac{e}{\hbar} (\mathbf{v}_{\mathbf{k}} \times \mathbf{B}) \frac{\partial}{\partial \mathbf{k}} \Psi_{M'}(\mathbf{k}) \qquad (20)$$

contains the Lorentz force, the scattering term

$$\mathcal{C}_{MM'} = \delta_{MM'} - N^{-1}(\mathcal{E}_{\mathrm{F}}) \sum_{\mathbf{k}, \mathbf{k}'} \delta(\mathcal{E}_{\mathbf{k}} - \mathcal{E}_{\mathrm{F}})$$

$$\times \Psi_M(\mathbf{k}) \tau_{\mathbf{k}} P_{\mathbf{k} \leftarrow \mathbf{k}'} \Psi_{M'}(\mathbf{k}') \qquad (21)$$

accounts for the scattering-in processes. The vectors

$$\mathbf{D}_M = N^{-1}(\mathcal{E}_{\mathrm{F}}) \sum_{\mathbf{k}} \delta(\mathcal{E}_{\mathbf{k}} - \mathcal{E}_{\mathrm{F}}) \Psi_M(\mathbf{k})$$

$$\times \tau_{\mathbf{k}} \, \eta_{\mathbf{k}}^{-1}(\mathbf{B}) \left[\mathbf{v}_{\mathbf{k}} + \frac{e}{\hbar} (\boldsymbol{\Omega}_{\mathbf{k}} \cdot \mathbf{v}_{\mathbf{k}}) \cdot \mathbf{B} \right] \qquad (22)$$

$$= \mathbf{D}_M^{\mathrm{I}} + \mathbf{D}_M^{\mathrm{II}} \qquad (23)$$

are sums of $\mathbf{D}_M^{\mathrm{I}}$ that include $\mathbf{v}_{\mathbf{k}}$ and $\mathbf{D}_M^{\mathrm{II}}$ that contain the term $e(\boldsymbol{\Omega}_{\mathbf{k}} \cdot \mathbf{v}_{\mathbf{k}})\mathbf{B}/\hbar$. The density of states (DOS) is given by $N(\mathcal{E}) = \sum_{\mathbf{k}} \delta(\mathcal{E}_{\mathbf{k}} - \mathcal{E})$.

The method of FSHs allows to calculate the mean free path up to arbitrary order in the Fermi velocity, which has the advantage that the unknown quantity $\boldsymbol{\Lambda}_{\mathbf{k}}$ is expressed in terms of the well-known group velocity. Further, the derivative of $\boldsymbol{\Lambda}_{\mathbf{k}}$, which is part of the Lorentz force term, is also expressed in terms of the FSHs and can thus be calculated analytically. Therefore, the Lorentz force term and the scattering-in term can be included easily in the solution of the Boltzmann equation.

IV. TRANSPORT PROPERTIES

Combining Eqs. (6), (9), (15), (18), and (19), we arrive at the charge current density

$$\mathbf{j} = - \frac{e}{V} \sum_{\mathbf{k}} \eta_{\mathbf{k}}^{-1} \left[\mathbf{v}_{\mathbf{k}} + \frac{e}{\hbar} \mathbf{E} \times \boldsymbol{\Omega}_{\mathbf{k}} + \frac{e}{\hbar} (\boldsymbol{\Omega}_{\mathbf{k}} \cdot \mathbf{v}_{\mathbf{k}}) \mathbf{B} \right]$$

$$\times \left(f_0 + \frac{\partial f^0}{\partial \mathcal{E}} e \boldsymbol{\Lambda}_{\mathbf{k}}(\mathbf{B}) \cdot \mathbf{E} \right) \qquad (24)$$

and

$$\boldsymbol{\Lambda}_{\mathbf{k}}(\mathbf{B}) = \sum_{M,M'} [(\mathcal{B} + \mathcal{C})^{-1}]_{MM'} \mathbf{D}_{M'} \Psi_M(\mathbf{k}). \qquad (25)$$

These expressions allow to distinguish individual contributions to the charge current and to clearly identify the terms related to the chiral anomaly. For this purpose, we split the mean free path into two parts, $\boldsymbol{\Lambda}_{\mathbf{k}}(\mathbf{B}) = \boldsymbol{\Lambda}_{\mathbf{k}}^{\mathrm{I}}(\mathbf{B}) + \boldsymbol{\Lambda}_{\mathbf{k}}^{\mathrm{II}}(\mathbf{B})$. $\boldsymbol{\Lambda}_{\mathbf{k}}^{\mathrm{I}}(\mathbf{B})$ and $\boldsymbol{\Lambda}_{\mathbf{k}}^{\mathrm{II}}(\mathbf{B})$ are defined by Eq. (25), in which $\mathbf{D}_{M'}$ is replaced by $\mathbf{D}_{M'}^{\mathrm{I}}$ and $\mathbf{D}_{M'}^{\mathrm{II}}$, respectively. This decomposition produces nine contributions to the charge current.

(1) $\mathbf{j}^{\mathrm{eq}} = - \frac{e}{V} \sum_{\mathbf{k}} \eta_{\mathbf{k}}^{-1} \mathbf{v}_{\mathbf{k}} f_0 = 0$ is an equilibrium contribution and vanishes for symmetry reasons.

(2) $\mathbf{j}^{\mathrm{AHE}} = - \frac{e^2}{V\hbar} \sum_{\mathbf{k}} \eta_{\mathbf{k}}^{-1} \mathbf{E} \times \boldsymbol{\Omega}_{\mathbf{k}} f_0$ represents the intrinsic anomalous Hall effect. It vanishes in systems with time-reversal symmetry.

(3) $\mathbf{j}^{\mathrm{CME}} = - \frac{e^2}{V\hbar} \sum_{\mathbf{k}} \eta_{\mathbf{k}}^{-1} (\boldsymbol{\Omega}_{\mathbf{k}} \cdot \mathbf{v}_{\mathbf{k}}) \mathbf{B} f_0$ corresponds to a charge current parallel to $\mathbf{B}$, which exists even in the absence of an electric field, that is an equilibrium chiral magnetic effect. It vanishes in systems with inversion or time-reversal symmetry. Its existence is controversially discussed [38–42]. However, it has been shown that this contribution is forbidden by gauge symmetry [43,44].

(4) $\mathbf{j}^{\mathrm{cl}} = - \frac{e^2}{V} \sum_{\mathbf{k}} \eta_{\mathbf{k}}^{-1} \mathbf{v}_{\mathbf{k}} \frac{\partial f_0}{\partial \mathcal{E}} [\boldsymbol{\Lambda}_{\mathbf{k}}^{\mathrm{I}}(\mathbf{B}) \cdot \mathbf{E}]$ is the conventional charge current including the Lorentz force, called *classical* in the following. Berry curvature-related effects enter via $\eta_{\mathbf{k}}$ in the matrix $\mathcal{B} + \mathcal{C}$.

(5) $\mathbf{j}^{\mathrm{linI}} = - \frac{e^3}{V\hbar} \sum_{\mathbf{k}} \eta_{\mathbf{k}}^{-1} (\boldsymbol{\Omega}_{\mathbf{k}} \cdot \mathbf{v}_{\mathbf{k}}) \mathbf{B} \frac{\partial f_0}{\partial \mathcal{E}} [\boldsymbol{\Lambda}_{\mathbf{k}}^{\mathrm{I}}(\mathbf{B}) \cdot \mathbf{E}]$ and $\mathbf{j}^{\mathrm{linII}} = - \frac{e^2}{V} \sum_{\mathbf{k}} \eta_{\mathbf{k}}^{-1} \mathbf{v}_{\mathbf{k}} \frac{\partial f_0}{\partial \mathcal{E}} [\boldsymbol{\Lambda}_{\mathbf{k}}^{\mathrm{II}}(\mathbf{B}) \cdot \mathbf{E}]$ are approximately linear

in **B** and exist only in systems with nonzero Berry curvature. Both terms have been discussed for systems with broken time-reversal symmetry in Refs. [24–26]. At first glance, they seem to vanish for time-reversal invariant systems, but the phase space correction $\eta_\mathbf{k}$ permits a finite contribution. For special geometries, both terms are equivalent.

$$(6) \quad \mathbf{j}^{\mathrm{2ndI}} = -\frac{e^3}{V\hbar}\sum_\mathbf{k}\eta_\mathbf{k}^{-1}(\mathbf{E}\times\boldsymbol{\Omega}_\mathbf{k})\frac{\partial f_0}{\partial\mathcal{E}}[\boldsymbol{\Lambda}_\mathbf{k}^{\mathrm{I}}(\mathbf{B})\cdot\mathbf{E}] \quad\text{and}$$

$\mathbf{j}^{\mathrm{2ndII}} = -\frac{e^3}{V\hbar}\sum_\mathbf{k}\eta_\mathbf{k}^{-1}(\mathbf{E}\times\boldsymbol{\Omega}_\mathbf{k})\frac{\partial f_0}{\partial\mathcal{E}}[\boldsymbol{\Lambda}_\mathbf{k}^{\mathrm{II}}(\mathbf{B})\cdot\mathbf{E}]$ are of second order in **E** and, thus, not considered in the linearized approach.

$(7)\ \mathbf{j}^{\mathrm{CA}} = -\frac{e^3}{V\hbar}\sum_\mathbf{k}\eta_\mathbf{k}^{-1}(\boldsymbol{\Omega}_\mathbf{k}\cdot\mathbf{v}_\mathbf{k})\mathbf{B}\frac{\partial f_0}{\partial\mathcal{E}}[\boldsymbol{\Lambda}_\mathbf{k}^{\mathrm{II}}(\mathbf{B})\cdot\mathbf{E}]$ refers to the contribution of the chiral anomaly [16]. It scales with B^2 and gives rise to a negative longitudinal magnetoresistance as well as a large planar Hall effect [45,46].

V. RESULTS AND DISCUSSION

We focus now on the nonequilibrium contributions $\mathbf{j}^{\mathrm{cl}}$, $\mathbf{j}^{\mathrm{linI}}$, $\mathbf{j}^{\mathrm{linII}}$, and $\mathbf{j}^{\mathrm{CA}}$ to the charge current and the corresponding charge conductivities $\hat\sigma$ in the presence of an external magnetic field. Beginning with simple systems, we increase the level of complexity to end up with TaAs.

A. Two isotropic Weyl points

For the discussion of the chiral anomaly, the isotropic Weyl Hamiltonian (1) is often employed for each Weyl point separately [16]. Neglecting the phase space correction and the scattering-in terms, a magnetic field $\mathbf{B} = (B_x, 0, 0)$ leads to the longitudinal charge conductivity [16]

$$\sigma_{xx} = \sigma_{xx}^{\mathrm{cl}} + \sigma_{xx}^{\mathrm{CA}} = \frac{e^2\tau_0(\mathcal{E}_\mathrm{F})\mathcal{E}_\mathrm{F}^2}{3\pi^2\hbar^3 v_0} + \frac{e^4 v_0^3 B_x^2\tau_0(\mathcal{E}_\mathrm{F})}{4\pi^2\hbar\mathcal{E}_\mathrm{F}^2}. \quad (26)$$

Here, $\hat\sigma^{\mathrm{linI}}$ and $\hat\sigma^{\mathrm{linII}}$ vanish for symmetry reasons because the phase space correction is neglected. The momentum relaxation time is isotropic on an isoenergy surface. Since τ_0 is not assumed constant but calculated as energy-dependent,

$$\tau_0(\mathcal{E}) = \frac{\pi\hbar^4 v_0^3}{|U|^2 c_i V_0\mathcal{E}^2}, \quad (27)$$

the longitudinal classical charge conductivity is constant in energy because the reduced density of states near the Weyl points is compensated by an increased momentum relaxation time. The chiral anomaly-related contribution scales with $\mathcal{E}^{-4}$. This is in contrast to the $\mathcal{E}^{-2}$ dependence found in literature [16,18], where τ_0 is taken as a parameter. Including the phase space correction would induce anisotropies of the momentum relaxation time and would therefore modify the results for $\sigma_{xx}^{\mathrm{cl}}$ and $\sigma_{xx}^{\mathrm{CA}}$; $\hat\sigma^{\mathrm{linI}}$ and $\hat\sigma^{\mathrm{linII}}$ may also be nonzero.

B. Two anisotropic Weyl points

A minimal inversion symmetric system of two Weyl points described by the model Hamiltonian (2) allows to demonstrate general and inversion symmetry-related features of the transport properties.

The chosen model parameters–$\gamma = 130\,\mathrm{eV}\,\text{Å}^2$, $m = 1.73 \times 10^{-4}\ \text{Å}^{-2}$, $v_y = v_z = 2.2\times10^5\,\mathrm{m/s}$–correspond approximately to those of a W1 point in TaAs (discussed below).
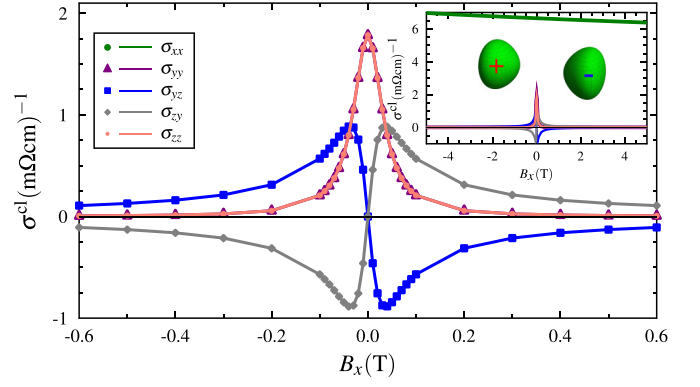
FIG. 2. Classical charge conductivity for a system of two Weyl points vs magnetic field applied in x direction, which is the direction of the Weyl dipole orientation (sketched by the green Fermi sheets). The inset shows the overview of all tensor elements for fields up to $\pm 5\mathrm{T}$, while the main figure provides details for small magnetic fields.

The Weyl cones are symmetric with respect to the k_y and k_z direction, but along k_x, that is the direction in which the Weyl points are separated, asymmetries occur. The Fermi energy is set to $\mathcal{E}_\mathrm{F} = 20\,\mathrm{meV}$, similar to the Fermi level of the TaAs W1 points, and lies below $\mathcal{E}_\mathrm{S}$.

For the calculation of the momentum relaxation time, the scattering potential is set constant to $U = 1\,\mathrm{eV}$, the impurity concentration is 1 at %, and the volume of the unit cell is $6\times6\times11\ \text{Å}^3$. These parameters enter the results as constant factors and are qualitatively insignificant for the results. The **k** points on the Fermi surface are calculated using an adaptive tetrahedral method. It turned out that FSHs up to $N = 3$ are sufficient since contributions from higher order FSHs are negligibly small.

1. Classical charge conductivity

The classical charge conductivity $\hat\sigma^{\mathrm{cl}}$ is shown in Fig. 2 for an external magnetic field $\mathbf{B} = (B_x, 0, 0)$, pointing in the direction of anisotropies in **k** space. For $B_x = 0$, the conductivity tensor is diagonal. $\sigma_{yy}^{\mathrm{cl}} = \sigma_{zz}^{\mathrm{cl}}$ are not equivalent to $\sigma_{xx}^{\mathrm{cl}}$ because of the anisotropic Fermi surface. With increasing B_x, the influence of the Lorentz force becomes pronounced. As expected from analytical model calculations [47], $\sigma_{yy}^{\mathrm{cl}}$ decreases with $-B_x^2$ for small fields, that is when scattering is dominant, and with B_x^{-2} for higher fields, forcing the electrons to move on cyclotron orbits.

The xx component provides an unconventional asymmetry with respect to B_x. For the highly symmetric system discussed here, it is expected to be constant in B_x. However, the asymmetry of the phase space correction factor with respect to $\mathbf{B}\leftrightarrow-\mathbf{B}$ for systems with broken time-reversal symmetry makes the momentum relaxation time also asymmetric in **B**. Symmetry dictates that $\tau_\mathbf{k}(\mathbf{B}) = \tau(k_x^2, \mathcal{E}, B_x)$. The magnetic field does not break inversion symmetry but influences the momentum relaxation time by coupling to the Berry curvature. Its influence on $\tau_\mathbf{k}$ is asymmetric with respect to $\mathbf{B}\leftrightarrow-\mathbf{B}$, which leads to asymmetries in the transport properties. A more detailed overview of the momentum relaxation time is given in Appendix A.
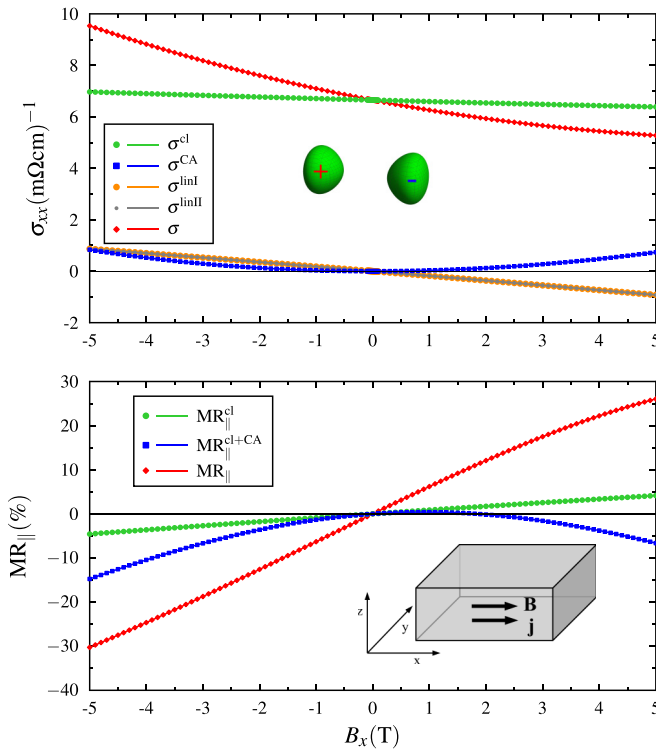
FIG. 3. Longitudinal transport properties for a system of two Weyl points separated in k_x direction for magnetic field applied in x direction. (Top) Charge conductivity σ_{xx}. The total charge conductivity as well as the individual contributions are shown. σ^{cl}, σ^{linI}, σ^{linII}, and σ^{CA}, are defined in Sec. IV. (Bottom) Longitudinal magnetoresistance $MR_\parallel$. The magnetoresistance considering only the classical charge conductivity (green) as well as the MR including σ^{cl} and σ^{CA} (blue) are shown. The LMR which takes into account all contributions to the charge conductivity is given in red. The inset sketches the sample with the directions of the magnetic field and the charge current.

The transversal (off-diagonal) components $\sigma_{yz}^{cl} = -\sigma_{zy}^{cl}$ represent the Hall effect. As expected from analytics [47], $\sigma_{yz}^{cl} \sim B_x$ for small fields, and $\sigma_{yz}^{cl} \sim B_x^{-1}$ for larger fields.

2. Berry curvature-related charge conductivity

For the considered system, the contributions $\hat{\sigma}^{linI}$, $\hat{\sigma}^{linII}$, and $\hat{\sigma}^{CA}$ to the charge conductivity that are related to the Berry curvature (defined in Sec. IV) have only nonzero xx components (depicted in the upper panel of Fig. 3).

σ_{xx}^{linI} and σ_{xx}^{linII} are identical. For this system with broken time-reversal symmetry, they can be of the same order as σ_{xx}^{CA}, which scales with B_x^2. From Fig. 3, it seems that σ_{xx}^{linI} and σ_{xx}^{linII} depend approximately linearly on the magnetic field. However, they also have a small symmetric contribution (approximately 3% of the antisymmetric one) due to the phase space correction. The sign of the linear term depends on the orientation of the magnetic field with respect to the Weyl point dipole moment: it vanishes if **B** is perpendicular to the Weyl dipole and changes sign if the Weyl points' chiralities or the magnetic field are reversed. The small symmetric contribution is negative if **B** is aligned with the Weyl dipole moment and positive if **B** is perpendicular to it. However, the sign of this

symmetric term is not a universal property but results from the specific model Hamiltonian used here.

Equation (24) tells that the contributions $\hat{\sigma}^{linI}$, $\hat{\sigma}^{linII}$, and $\hat{\sigma}^{CA}$ are not a direct consequence of the nonzero chirality but result from the nonvanishing Berry curvature of the states. Therefore, these terms contribute also in energy regions in which the Weyl points' Fermi surfaces are connected (there $\chi = 0$). Since the Berry curvature scales approximately with $\mathcal{E}^{-2}$, these are however comparably small.

The energy-dependent charge conductivity for an anisotropic system of two Weyl points is shown in Appendix B. As in the isotropic Weyl model, σ_{xx}^{cl} is approximately constant with respect to $\mathcal{E}$. The Berry curvature-related contribution σ_{xx}^{CA} scales with $\approx \mathcal{E}^{-4}$, as in the isotropic model. Deviations occur near the Weyl point energy because of the enhanced phase space correction factor.

3. Longitudinal magnetoresistance

To demonstrate the influence of $\hat{\sigma}^{linI}$ and $\hat{\sigma}^{linII}$, the LMR is decomposed as shown in the lower panel of Fig. 3. First, only the classical charge conductivity is considered. Due to the phase space correction, the MR is not symmetric with respect to B_x. The second curve represents the LMR for which σ_{xx}^{cl} as well as σ_{xx}^{CA} are taken into account. The LMR is dominated by the term σ_{xx}^{CA}, which increases with B_x^2 and leads to a NLMR, as discussed in literature [16]. The third curve includes all contributions. Due to the nearly linear B_x dependences of σ_{xx}^{linI} and σ_{xx}^{linII}, the LMR is asymmetric with respect to B_x, and the additional contributions can induce a sign change. However, for fields larger than those shown in Fig. 3, the quadratic contribution σ_{xx}^{CA} dominates and the LMR becomes negative.

By exchanging the positions of the Weyl points, that is a reversal of the Weyl dipole moment, the sign of the Berry curvature is reversed at each **k**. Since the magnetic field couples to the Berry curvature, this exchange has the same effect on the longitudinal transport properties as a reversal of the magnetic field.

C. Four anisotropic Weyl points

A minimal time-reversal symmetric system of four Weyl points is discussed in this section; we take the same model parameters as before. The classical charge conductivity shows qualitatively the same B_x dependence as the system of two Weyl points (not shown here). The only difference is that for four Weyl points the longitudinal charge conductivity σ_{xx}^{cl} is symmetric and increases slightly with $|B_x|$. As before, this B_x dependence originates from the phase space correction which is invariant under $(\mathbf{B} \leftrightarrow -\mathbf{B}) \wedge (\mathbf{k} \leftrightarrow -\mathbf{k})$. Further, the energy dependencies are identical to those of the two Weyl points system (see Appendix B).

The slight increase with $|B_x|$ of the classical contribution is irrelevant (upper panel of Fig. 4), σ_{xx}^{CA} scales with B_x^2. Without the phase space correction, σ_{xx}^{linI} and σ_{xx}^{linII} would vanish because of time-reversal symmetry. However, since the applied magnetic field breaks this symmetry and couples to the Berry curvature, these terms can be nonzero (this feature is illustrated by means of the **k**-dependent momentum relaxation time in Appendix A). For $\mathbf{B} = 0$, the momentum relaxation time is constant on an isoenergy surface. If time-reversal
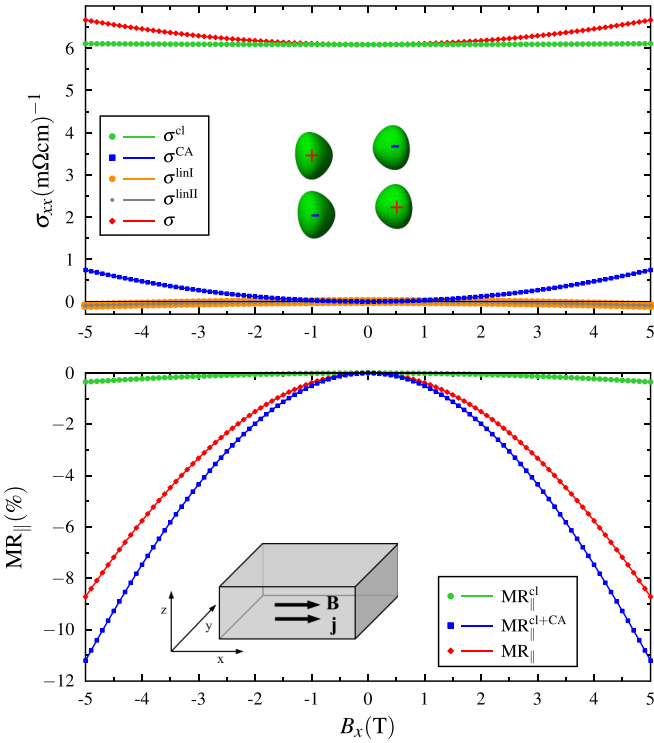
FIG. 4. As Fig. 3 but for a system with four Weyl points (see sketch of the Fermi surfaces).

symmetry is broken by the magnetic field, the momentum relaxation time becomes anisotropic, $\tau_{\mathbf{k}} \neq \tau_{-\mathbf{k}}$, which allows finite contributions $\sigma_{xx}^{\mathrm{linI}}$ and $\sigma_{xx}^{\mathrm{linII}}$. For the chosen parameters these are negative, small, and scale approximately as $-B_x^2$; their absolute value is up to 20% of $\sigma_{xx}^{\mathrm{CA}}$. Thus they compensate partially the contribution $\sigma_{xx}^{\mathrm{CA}}$ but do not induce a sign change of the LMR. Recall that in general $\sigma_{xx}^{\mathrm{linI}}$ and $\sigma_{xx}^{\mathrm{linII}}$ can be positive, depending on the orientation of $\mathbf{B}$: they are negative if $\mathbf{B}$ is oriented in the direction of Weyl point separation and become positive of $\mathbf{B}$ is perpendicular to that direction because of the scattering-in terms. However, in general, the sign of $\sigma_{ij}^{\mathrm{linI}}$ and $\sigma_{ij}^{\mathrm{linII}}$ in a time-reversal symmetric system also depends on the specific model Hamiltonian.

As a result, the LMR is negative (lower panel of Fig. 4), and its B_x dependence agrees with that derived in Ref. [16]. It is thus evident that the additional terms modify the magnitude of the NLMR but do not change its qualitative B_x dependence.

D. TaAs

The theory, so far applied to systems with two or four Weyl points, is now extended to a more realistic system: the type-I time-reversal symmetric Weyl semimetal TaAs [48–55] which hosts 24 Weyl points near the Fermi level. The band structure in the vicinity of these points is approximated by the model Hamiltonian (2) using the parameters derived in Ref. [12] from Ref. [51] (reproduced in Table I).

The Weyl points, separated into eight Weyl points of class W1 and 16 Weyl points of class W2, are arranged in groups of eight in three planes parallel to the $k_z = 0$ plane; one of these planes is sketched in the inset of Fig. 5. The Cartesian axes x, y, and z are parallel to the [100], [010], and [001]

TABLE I. Model parameters for the TaAs band structure close to the W1 and W2 Weyl points (adapted from Ref. [51]). $\mathcal{E}_{\mathrm{FW}}$ is the energy distance from the Fermi level to the Weyl points.

	Number	$\mathcal{E}_{\mathrm{FW}}$ (meV)	$\mathcal{E}_{\mathrm{S}}$ (meV)	v_y (10^5 m/s)	v_z (10^5 m/s)	m_0 (10^{-4} Å^{-2})	γ (eVÅ^2)
W1	8	22.1	22.5	2.2	0.2	1.73	130
W2	16	8.9	47.9	2.6	3.1	11.4	42

directions, respectively. The Fermi surface is invariant with respect to fourfold rotations about the z axis.

1. Energy dependence of the conductivity

Since the B_x dependence of the contributions to the charge conductivity is qualitatively equivalent to those for four Weyl points, we focus on the energy dependence of the transport coefficients. Due to the complicated arrangement of Weyl points, this dependence is not as simple as for two or four Weyl points.

For $\mathbf{B} = 0$, σ_{xx} and σ_{yy} are equivalent for symmetry reasons, whereas σ_{zz} is strongly reduced (Fig. 5). The low σ_{zz} value results from the asymmetry of the Fermi surface: the W1 Fermi surfaces are strongly extended in k_z direction leading to a low charge conductivity. The longitudinal charge conductivities are almost constant because the energy dependencies of DOS and momentum relaxation time approximately compensate. Due to the Lifshitz transition, at $\mathcal{E}_{\mathrm{S}}^{(1)}$ (saddle point of W1) a step occurs. Here, the DOS exhibits a Van Hove singularity, $N(\mathcal{E}) \propto \sqrt{\mathcal{E}_{\mathrm{S}} - \mathcal{E}}$ ($\mathcal{E} < \mathcal{E}_{\mathrm{S}}$) leading to a steplike energy dependence of τ and $\hat{\sigma}$.

The presence of a magnetic field in x direction ($B_x = 2$ T) leads to a decrease of σ_{yy} and σ_{zz} because of the Lorentz force. The amount of reduction depends strongly on the energy; at energies near the Weyl points, the scattering rates are low, the electrons move along the isoenergy orbits almost unperturbed by scattering. Thus, the influence of the Lorentz force is pronounced (strong fields). At higher energies, scattering
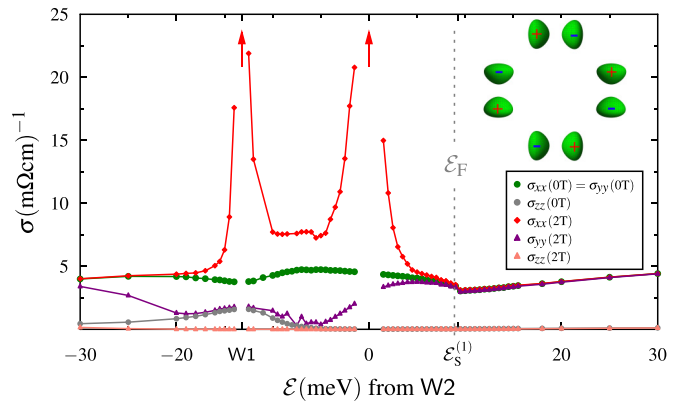
FIG. 5. Charge conductivities σ_{xx}, σ_{yy}, and σ_{zz} of TaAs vs energy without ($B = 0$) and with ($B_x = 2$ T) magnetic field, respectively. The positions of W1 and W2 as well as the associated saddle point $\mathcal{E}_{\mathrm{S}}^{(1)}$ are indicated. $\mathcal{E}_{\mathrm{S}}^{(2)}$ is not within the depicted energy range. The gray dashed line marks the position of the Fermi level. The inset sketches the eight W1 points that lie in the $k_z = 0$ plane.
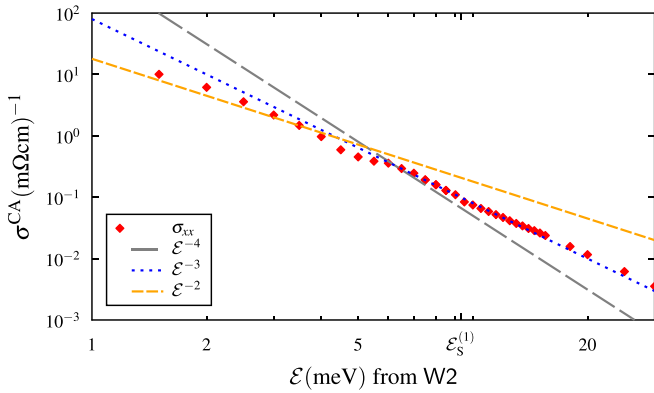
FIG. 6. Energy dependence of the Berry curvature-related contribution σ_{xx}^{CA} for $B_x = 1$ T for energies above the W2 energy. The double logarithmic plot shows that σ_{xx}^{CA} scales approximately with $\mathcal{E}^{-3}$ (dashed).

FIG. 7. LMR of TaAs. The magnetic field is applied in the x ($B \parallel x$) and z ($B \parallel z$) direction, respectively. In addition, it is slightly tilted by $1°$ of the crystal axes within the xz plane (inset). The current for detecting the LMR is always parallel to the magnetic field.

dominates, the influence of the magnetic field on the electrons is less distinct (weak fields).

The most noticeable effect of the magnetic field is the strong increase of the longitudinal charge conductivity σ_{xx} due to the chiral anomaly. The additional contributions are maximum around the W1 and W2 points.

The qualitative energy dependence of the Berry curvature-related σ_{xx}^{CA} is examined by a double logarithmic representation for energies above the W2 energy (Fig. 6). In general, the data points follow an $\mathcal{E}^{-3}$ dependence. Closer to the Weyl points, an $\mathcal{E}^{-2}$ dependence seems as well reasonable, which would support data observed by Zhang *et al.* [18]. The $\mathcal{E}^{-4}$ dependence calculated for Weyl points at a single energy is not reproduced because the different energies of the W1 and W2 points result in a complicated scattering behavior. A similar energy dependence is found for energies below W1 (not shown here). In between the energies of W1 and W2, σ_{xx}^{CA} is nearly constant because of the energy overlap of the Weyl cones. The energy dependence of σ_{xx}^{linI} and σ_{xx}^{linII} (not shown here) reminds to that of σ_{xx}^{CA}. At $\mathcal{E}_F$, the contributions σ_{xx}^{linI} and σ_{xx}^{linII} are $\approx 4.5\%$ of σ_{xx}^{CA}. Here, the large number of Weyl points and the fourfold rotational symmetry of the Fermi surface lead to a reduction of these anisotropy related terms, as discussed in Appendix A.

The semiclassical approach is not appropriate for energies closer to the Weyl points than about 1 meV because of interband contributions and lifetime broadening, which are not taken into account [12]. Within this narrow energy region, a Kubo approach is appropriate. On top of this, the phase space correction term diverges at the Weyl points, thereby increasing numerical errors. We estimate the energy range around the Weyl points in which the semiclassical Boltzmann method cannot be safely applied to ± 1 meV for W1 and ± 2.5 meV for W2, respectively. Within this energy range, the phase space correction factor is > 100 for magnetic fields up to 10 T.

2. Angular dependence of the LMR

The Fermi level in TaAs given in Ref. [51] and used throughout this paper (Table I) is not very close to the Weyl points. Thus the chiral anomaly-related charge conductivity is
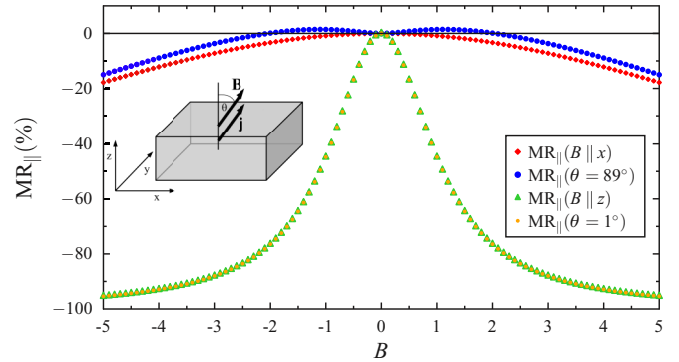
not extraordinary large. However, due to the B^2 dependence, a clear NLMR signal is calculated at the Fermi level.

For **B** in the direction of one of the Cartesian axes of the system, the LMR is negative because the chiral-anomaly terms dominate the B dependence of the charge conductivity (Fig. 7). However, if **B** is tilted off the x axis by $1°$ ($\theta = 89°$), a PLMR is observed for fields less than 2 T. This B dependence resembles the data measured in various experiments [18–22] for which the PLMR at small fields is usually explained by weak antilocalization [33]. Interestingly, the PLMR calculated here occurs only if **B** is nearly parallel to the x axis, but not if **B** is slightly tilted off the z axis.

In order to understand the conditions under which a PLMR occurs for misaligned **B**, we examine the magnetoresistance parallel to the crystal axes—MR_{xx}, MR_{yy}, and MR_{zz}, defined as $MR_{ii} = (\rho_{ii}(\mathbf{B}) - \rho_{ii}(0))/\rho_{ii}(0)$ with $\hat{\rho}$ the resistivity tensor—as a function of the **B** direction (Fig. 8). The magnetic field is set to $B = 1.5$ T and is rotated by θ within the xz plane. In what follows, the labels longitudinal and transversal refer to the orientation of the charge current with respect to the magnetic field.
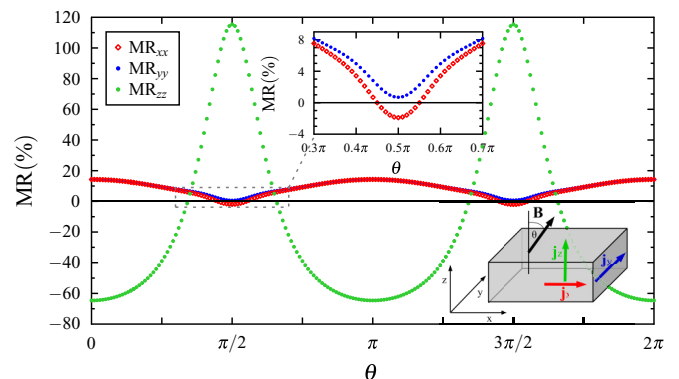
FIG. 8. Magnetoresistance (MR) along the three crystal axes x, y, and z as a function of the angle θ of the magnetic field **B**. The field is rotated in the xz plane, with $\theta = 0$ corresponds to $\mathbf{B} \parallel z$ and $\theta = \pi/2$ corresponds to $\mathbf{B} \parallel x$ (see sketch). The absolute value of **B** is 1.5 T. The inset depicts details around $\theta = \pi/2$.

MR_{yy} is always transversal and positive, the latter explained by the fact that only the classical charge conductivity contributes, which is strongly influenced by the Lorentz force, and the chiral anomaly-related terms vanish. The oscillations with θ originate from the anisotropy of the Fermi surfaces.

MR_{xx} and MR_{zz} have both longitudinal as well as transversal components, depending on the direction of **B**. For symmetry reasons, $MR_{xx} = MR_{yy}$ if **B** $\parallel z$. If $B_x \neq 0$, the chiral anomaly produces a negative contribution to MR_{xx}, whereas the Lorentz force contributes positively to the magnetoresistance. For θ near $\pi/2$, the contributions from the chiral anomaly dominate the classical term, and MR_{xx} becomes negative. For the same reason, MR_{zz} is negative for θ near 0 and positive around $\theta = \pi/2$.

Importantly, the amplitude of MR_{zz} is larger than those of MR_{xx} and MR_{yy} because of the anisotropy of the Fermi surfaces. The Fermi surfaces are elongated in z direction which leads to a small σ_{zz}, a large resistivity ρ_{zz}, and a large magnetoresistance MR_{zz} in z direction: the relative change of resistivity is more pronounced in z direction. Due to this anisotropy of the system, the amplitudes of MR_{zz} are enhanced and the angular region with $MR_{zz} < 0$, which means the chiral anomaly dominates the sign of MR_{zz}, is larger than the region with $MR_{xx} < 0$.

The LMR, which is associated with the current in the direction of the magnetic field, is the projection of the magnetoresistivity onto the direction of **B** and therefore contains components of MR_{xx} as well as MR_{zz},

$$MR_{\parallel}(\mathbf{B}) = \big(MR_{xx}(\mathbf{B})\rho_{xx}^0 \sin^2\theta + MR_{zz}(\mathbf{B})\rho_{zz}^0 \cos^2\theta$$
$$+ 2\rho_{xz}(\mathbf{B})\sin\theta\cos\theta\big)\big/\big(\rho_{xx}^0 \sin^2\theta + \rho_{zz}^0 \cos^2\theta\big),$$
$$(28)$$

with ρ_{xx} and ρ_{zz} are diagonal elements of the resistivity tensor $\hat{\rho}$. The superscript 0 refers to $\hat{\rho}(\mathbf{B} = 0)$. The influence of the nondiagonal elements of $\hat{\rho}(\mathbf{B})$ is less important here and will be neglected in the qualitative discussion.

For **B** with $\theta \approx 0$ or $\approx \pi$, the negative contribution from MR_{zz} (originating from the chiral anomaly) dominates the classical positive contribution from MR_{xx} (Lorentz force contribution) in a wide angular range. Thus, even if the magnetic field is tilted by $10°$, the LMR would be negative for $B = 1.5$ T. By contrast, around $\theta = \pi/2$ or $3\pi/2$, the positive MR_{zz} component dominates over the negative MR_{xx} component already for a tilt angle of $1°$, leading to a PLMR.

In other words, due to the Lorentz force, the charge current is not aligned with the electric field. Since the current direction is fixed to be parallel to **B** by definition of the longitudinal MR, **E** and **B** are not parallel, which reduces the chiral anomaly-related transfer of states between the Weyl cones and consequently also the associated charge conductivity. Thus the classical PLMR contribution can dominate the total LMR for small magnetic fields, whereas for larger fields the chiral anomaly contribution is sufficiently large to induce a total negative LMR signal. Hence, the PLMR for small tilt angles is a consequence of including the Lorentz force term in the Boltzmann equation. Revealing this feature is one of the main advantages of using the Fermi surface harmonics approach.

The above discussed PLMR is not a specific property of TaAs but can in general occur in any Weyl system with anisotropic Fermi surfaces. However, its magnitude as well as the tilt angle under which the PLMR occurs strongly depend on the specific properties of the system. In general, for Fermi energies close to the Weyl points the chiral anomaly is expected to be the dominant term leading to a NLMR whereas for energies further away from the Weyl points the Lorentz force can lead to a more pronounced PLMR.

In Ref. [18], Zhang *et al.* present measurements of the LMR of five different TaAs samples with various Fermi levels. The magnetic field and the electric charge current are pointing in x and z direction, respectively. For both experimental geometries, the characteristic curves show a PLMR for small fields and a NLMR for larger fields attributed to weak antilocalization and the chiral anomaly, respectively.

As discussed above, a slight tilt of the magnetic field and the charge current off the crystal symmetry axes could also give rise to the characteristic curves measured in Ref. [18]. However, as our calculations show, these features occur only if **B** is slightly tilted off the x direction, but not if **B** is almost parallel to z. Further, all transport properties depend strongly on the Fermi level since the DOS of a Weyl pair vanishes at the Weyl point energy. The Fermi levels observed for the samples of Ref. [18] are almost all closer than 5 meV to the W2 points. For these energies, our model calculations do not show a pronounced PLMR for tilt angles up to $5°$. Thus we conclude that a slight tilt of the sample cannot be the reason for the observed PLMR, what supports the argument of the weak antilocalization.

VI. CONCLUSION

In this work, we derived a Fermi surface harmonics (FSHs) formalism for solving the semiclassical Boltzmann transport equation for systems with nonvanishing Berry curvature in the presence of electric and magnetic fields. This method provides an elegant way to account for scattering-in terms, Lorentz force term and phase space corrections.

As applications, we calculated the transport properties for different Weyl systems. Taking into account the energy dependence of the relaxation time qualitatively modifies the energy dependence of the chiral anomaly-related charge conductivity from $\mathcal{E}^{-2}$ to $\mathcal{E}^{-4}$ in isotropic systems. We identified contributions to the charge conductivity that scale linearly with B and can change the sign of the magnetoresistance in systems with broken time-reversal symmetry. These anisotropy-related terms are less pronounced in time-reversal symmetric systems with a large number of Weyl points.

Further, a slight tilt of the **B** field with respect to the crystal axes can give rise to a PLMR for small magnetic fields, with a signal similar to the PLMR induced by weak antilocalization. Nevertheless, for the Weyl semimetal TaAs, these tilting effects appear not to reproduce the PLMR observed in experiments with small fields.

The presented method is not restricted to Weyl semimetals but can be applied to many more systems, especially to any topological materials with nonzero Berry curvature. The method could also be used for a more detailed analysis of the planar Hall effect; the latter is included in the formalism
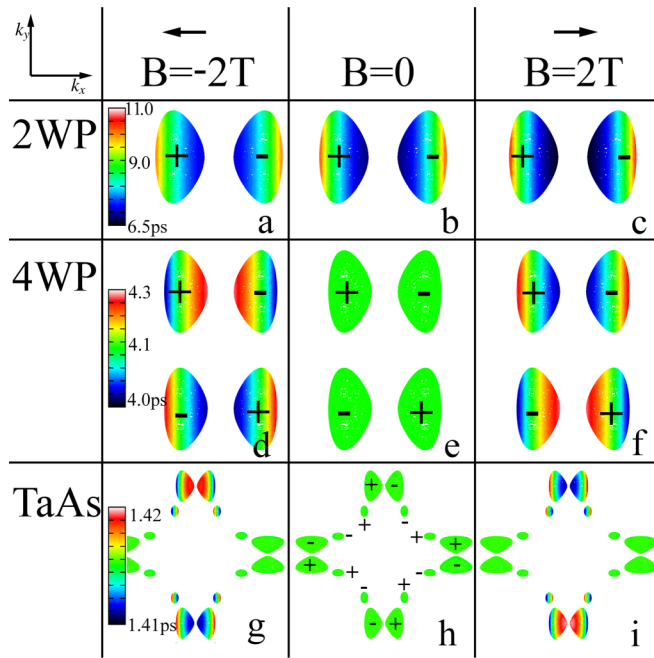
FIG. 9. Momentum relaxation time (color scale) for a system of two Weyl points [(a)–(c)], four Weyl points [(d)–(f)], and TaAs [(g)–(i)]. The relaxation time is calculated on the iso-energy surfaces and projected onto the $k_x k_y$ plane. Therefore, for TaAs, 16 of the 24 Weyl points are visible. The magnetic field of ± 2 T is assumed in $\pm x$ direction, respectively. The color scale differs for each row but rows share a common color scale.

FIG. 10. Longitudinal charge conductivity vs energy for systems with two and four Weyl points. The Weyl point energy is at $\mathcal{E} = 0$, the magnetic field reads $\mathbf{B} = (1\,\mathrm{T}, 0, 0)$. (Top) Classical charge conductivity $\sigma_{xx}^{\mathrm{cl}}$. (Bottom) Chiral anomaly-related contribution $\sigma_{xx}^{\mathrm{CA}}$ in a double-logarithmic representation.

but its discussion is beyond the purpose of this paper. In future work, the FSH formalism may be extended to surface states in order to study their contributions to the transport properties.

Note added. During the course of the review process, a paper considering the chiral anomaly and the Lorentz force in isotropic Weyl systems within a Fourier harmonics approach for solving the Boltzmann equation was published [56]. In contrast to Ref. [56], we calculate the momentum relaxation time **k** and $\mathcal{E}$ dependently, include scattering-in processes as well as anisotropies of the system and discuss TaAs as a realistic system.

APPENDIX A: MOMENTUM RELAXATION TIME IN THE PRESENCE OF A MAGNETIC FIELD

The momentum relaxation time $\tau_{\mathbf{k}}$ is calculated from Eq. (11) and depicted in Fig. 9 for systems hosting two and four Weyl points as well as TaAs (24 Weyl points). In general, the relaxation time decreases with increasing number of Weyl points due to the enhanced phase space for scattering.

For $B = 0$, the momentum relaxation time is isotropic for systems with time-reversal symmetry, which is the four Weyl points system (e) and TaAs (h), in line with the symmetries of the Hamiltonian and its eigenstates. When time-reversal

symmetry is broken, as for a system of two Weyl points (b), anisotropies along the k_x direction show up, that is along the Weyl dipole moment.

A magnetic field enters the momentum relaxation time via the phase space correction factor when the integration in **k** space is performed; confer Eq. (16). Therefore the momentum relaxation time becomes **B**-dependent. Symmetry dictates that only the component of the magnetic field in the direction of the Weyl point separation (direction of Weyl pair dipole moment) influences the momentum relaxation time. Further, $\tau_{\mathbf{k}}$ varies only in the Weyl dipole direction and is constant on planes perpendicular to this direction. This finding is a special property of the model Hamiltonian.

In the inversion symmetric system of two Weyl points, the momentum relaxation time is slightly changed by the magnetic field (top row). If the magnetic field is pointing in the direction of the Weyl dipole [pointing from $\chi = -1$ to $\chi = 1$, (a)], the anisotropy of the momentum relaxation time is in general less pronounced, whereas it is more distinct when **B** is antiparallel to the Weyl dipole moment (c). This asymmetry of the momentum relaxation time with respect to B_x explains the asymmetric behavior of the transport properties discussed in Sec. V B.

In the systems with four Weyl points (center row) and in TaAs (bottom row), the time-reversal symmetry is broken by the magnetic field. Therefore $\tau_{\mathbf{k}} \neq \tau_{-\mathbf{k}}$. This symmetry breaking is the reason for nonzero additional contributions $\sigma_{xx}^{\mathrm{linI}}$ and $\sigma_{xx}^{\mathrm{linII}}$ to the charge conductivity, which vanish if

time-reversal symmetry is conserved. The influence of the magnetic field on $\tau_{\mathbf{k}}$ depends on the orientation of **B** with respect to each Weyl pair's dipole moment, as shown in (d), (f), (g), and (i), respectively.

For TaAs, whose 24 Weyl points are arranged symmetric with respect to the x and y axes, it becomes evident [(g) and (i)] that the magnetic field influences only the momentum relaxation time of the Weyl point pairs separated in the direction of the magnetic field (x). The influence of the magnetic field becomes less pronounced here because due to the fourfold rotational symmetry of the Fermi surface, the phase space for scattering and the number of scattering processes that are not affected by the phase space correction is enhanced. Thus, the anisotropy-related charge conductivity contributions $\hat{\sigma}^{\text{linI}}$ and $\hat{\sigma}^{\text{linII}}$ are reduced due to the larger number of Weyl points.

APPENDIX B: ENERGY DEPENDENCE OF CHARGE CONDUCTIVITIES

We focus on systems with two and four Weyl points modeled by the Hamiltonian (2). As expected from the isotropic model, the classical charge conductivity is almost constant with respect to the Fermi level (top in Fig. 10). The increase near the Weyl points originates from the enhanced phase space correction factor. The numerical values for the system of two and four Weyl points are close to each other. The larger number of contributing states (phase space) in the system with four Weyl points is compensated by a smaller momentum relaxation time. The longitudinal contribution σ_{xx}^{CA} related to the chiral anomaly exhibits a clear $\mathcal{E}^{-4}$ dependence (bottom), confirming analytical calculations for the isotropic model.

[1] S. Murakami, New J. Phys. **9**, 356 (2007).
[2] X. Wan, A. M. Turner, A. Vishwanath, and S. Y. Savrasov, Phys. Rev. B **83**, 205101 (2011).
[3] K.-Y. Yang, Y.-M. Lu, and Y. Ran, Phys. Rev. B **84**, 075129 (2011).
[4] A. A. Burkov and L. Balents, Phys. Rev. Lett. **107**, 127205 (2011).
[5] S.-Y. Xu, I. Belopolski, N. Alidoust, M. Neupane, G. Bian, C. Zhang, R. Sankar, G. Chang, Z. Yuan, C.-C. Lee, S.-M. Huang, H. Zheng, J. Ma, D. S. Sanchez, B. Wang, A. Bansil, F. Chou, P. P. Shibayev, H. Lin, S. Jia, and M. Z. Hasan, Science **349**, 613 (2015).
[6] H. Weyl, Z. Phys. **56**, 330 (1929).
[7] H. Nielsen and M. Ninomiya, Phys. Lett. B **105**, 219 (1981).
[8] H. Nielsen and M. Ninomiya, Nucl. Phys. B **185**, 20 (1981).
[9] H. Nielsen and M. Ninomiya, Nucl. Phys. B **193**, 173 (1981).
[10] P. Hosur and X. Qi, C. R. Phys. **14**, 857 (2013).
[11] A. A. Burkov, Phys. Rev. Lett. **113**, 187202 (2014).
[12] A. Johansson, J. Henk, and I. Mertig, Phys. Rev. B **97**, 085417 (2018).
[13] S. L. Adler, Phys. Rev. **177**, 2426 (1969).
[14] J. S. Bell and R. Jackiw, Il Nuovo Cimento A **60**, 47 (1969).
[15] H. Nielsen and M. Ninomiya, Phys. Lett. B **130**, 389 (1983).
[16] D. T. Son and B. Z. Spivak, Phys. Rev. B **88**, 104412 (2013).
[17] B. Z. Spivak and A. V. Andreev, Phys. Rev. B **93**, 085107 (2016).
[18] C.-L. Zhang, S.-Y. Xu, I. Belopolski, Z. Yuan, Z. Lin, B. Tong, G. Bian, N. Alidoust, C.-C. Lee, S.-M. Huang, T.-R. Chang, G. Chang, C.-H. Hsu, H.-T. Jeng, M. Neupane, D. S. Sanchez, H. Zheng, J. Wang, H. Lin, C. Zhang, H.-Z. Lu, S.-Q. Shen, T. Neupert, M. Z. Hasan, and S. Jia, Nat. Commun. **7**, 10735 (2016).
[19] H.-J. Kim, K.-S. Kim, J.-F. Wang, M. Sasaki, N. Satoh, A. Ohnishi, M. Kitaura, M. Yang, and L. Li, Phys. Rev. Lett. **111**, 246603 (2013).
[20] J. Xiong, S. K. Kushwaha, T. Liang, J. W. Krizan, M. Hirschberger, W. Wang, R. J. Cava, and N. P. Ong, Science **350**, 413 (2015).
[21] C. Z. Li, L. X. Wang, H. Liu, J. Wang, Z. M. Liao, and D. P. Yu, Nat. Commun. **6**, 10137 (2015).
[22] Q. Li and D. E. Kharzeev, Nucl. Phys. A **956**, 107 (2016).

[23] M. Hirschberger, S. Kushwaha, Z. Wang, Q. Gibson, S. Liang, C. A. Belvin, B. A. Bernevig, R. J. Cava, and N. P. Ong, Nat. Mater. **15**, 1161 (2016).
[24] A. Cortijo, Phys. Rev. B **94**, 241105 (2016).
[25] G. Sharma, P. Goswami, and S. Tewari, Phys. Rev. B **96**, 045112 (2017).
[26] V. A. Zyuzin, Phys. Rev. B **95**, 245128 (2017).
[27] S. Liang, J. Lin, S. Kushwaha, J. Xing, N. Ni, R. J. Cava, and N. P. Ong, Physi. Rev. X **8**, 031002 (2018).
[28] Z. Li, Y. Zeng, J. Zhang, M. Zhou, and W. Wu, Phys. Rev. B **98**, 165441 (2018).
[29] P. B. Allen, Phys. Rev. B **13**, 1416 (1976).
[30] I. Mertig and E. Mrosan, J. Phys. F **12**, 3031 (1982).
[31] I. Mertig, E. Mrosan, and P. Ziesche, *Multiple Scattering Theory of Point Defects in Metals: Electronic Properties*, Teubner-Texte zur Physik (Teubner Verlagsgesellschaft, Leipzig, 1986).
[32] D. Xiao, J. Shi, and Q. Niu, Phys. Rev. Lett. **95**, 137204 (2005).
[33] H.-Z. Lu and S.-Q. Shen, Phys. Rev. B **92**, 035203 (2015).
[34] S. Murakami and S.-i. Kuga, Phys. Rev. B **78**, 165313 (2008).
[35] R. Okugawa and S. Murakami, Phys. Rev. B **89**, 235315 (2014).
[36] H. Rostami and M. Polini, Phys. Rev. B **97**, 195151 (2018).
[37] G. Sundaram and Q. Niu, Phys. Rev. B **59**, 14915 (1999).
[38] A. A. Zyuzin and A. A. Burkov, Phys. Rev. B **86**, 115133 (2012).
[39] A. A. Zyuzin, S. Wu, and A. A. Burkov, Phys. Rev. B **85**, 165110 (2012).
[40] A. A. Burkov, Phys. Rev. Lett. **113**, 247203 (2014).
[41] A. Cortijo, D. Kharzeev, K. Landsteiner, and M. A. H. Vozmediano, Phys. Rev. B **94**, 241405 (2016).
[42] A. A. Burkov, Phys. Rev. B **91**, 245157 (2015).
[43] Y. V. Nazarov, JETP **64**, 193 (1986).
[44] M. A. Zubkov, Phys. Rev. D **93**, 105036 (2016).
[45] S. Nandy, G. Sharma, A. Taraphder, and S. Tewari, Phys. Rev. Lett. **119**, 176804 (2017).
[46] A. A. Burkov, Phys. Rev. B **96**, 041110 (2017).
[47] W. Brauer, *Einführung in die Elektronentheorie der Metalle* (Springer Fachmedien, Wiesbaden, 2013).
[48] S.-M. Huang, S.-Y. Xu, I. Belopolski, C.-C. Lee, G. Chang, B. Wang, N. Alidoust, G. Bian, M. Neupane, C. Zhang, S. Jia, A. Bansil, H. Lin, and M. Z. Hasan, Nat. Commun. **6**, 7373 (2015).
[49] L. X. Yang, Z. K. Liu, Y. Sun, H. Peng, H. F. Yang, T. Zhang, B. Zhou, Y. Zhang, Y. F. Guo, M. Rahn, D. Prabhakaran, Z.

Hussain, S.-K. Mo, C. Felser, B. Yan, and Y. L. Chen, Nat. Phys. **11**, 728 (2015).

[50] H. Weng, C. Fang, Z. Fang, B. A. Bernevig, and X. Dai, Phys. Rev. X **5**, 011029 (2015).

[51] C.-C. Lee, S.-Y. Xu, S.-M. Huang, D. S. Sanchez, I. Belopolski, G. Chang, G. Bian, N. Alidoust, H. Zheng, M. Neupane, B. Wang, A. Bansil, M. Z. Hasan, and H. Lin, Phys. Rev. B **92**, 235104 (2015).

[52] Y. Sun, S.-C. Wu, and B. Yan, Phys. Rev. B **92**, 115428 (2015).

[53] B. Q. Lv, H. M. Weng, B. B. Fu, X. P. Wang, H. Miao, J. Ma, P. Richard, X. C. Huang, L. X. Zhao, G. F. Chen, Z. Fang, X. Dai, T. Qian, and H. Ding, Phys. Rev. X **5**, 031013 (2015).

[54] S.-Y. Xu, I. Belopolski, D. S. Sanchez, M. Neupane, G. Chang, K. Yaji, Z. Yuan, C. Zhang, K. Kuroda, G. Bian, C. Guo, H. Lu, T.-R. Chang, N. Alidoust, H. Zheng, C.-C. Lee, S.-M. Huang, C.-H. Hsu, H.-T. Jeng, A. Bansil, T. Neupert, F. Komori, T. Kondo, S. Shin, H. Lin, S. Jia, and M. Z. Hasan, Phys. Rev. Lett. **116**, 096801 (2016).

[55] F. Arnold, M. Naumann, S.-C. Wu, Y. Sun, M. Schmidt, H. Borrmann, C. Felser, B. Yan, and E. Hassinger, Phys. Rev. Lett. **117**, 146401 (2016).

[56] M. Imran and S. Hershfield, Phys. Rev. B **98**, 205139 (2018).